**Abstract** Periodic arrays of plasmonic nanoantennas can enhance the directionality of light emission of nearby fluorophores and, therefore, have a great potential for a broad range of applications. Unfortunately, their narrow spectral bandwidth and the anisotropy of their optical resonances limit the use of these structures in applications such as solid state lighting. In this article, we study an alternative for periodic structures: Vogel's golden spirals. These spirals are deterministic structures with an approximate circular symmetry and a Fourier transform that is much more broadband than that of periodic lattices. Combining k-space polarimetry and theoretical calculations, we first investigate the light scattering from Vogel's arrays and the coupling between individual nanoantennas. Next, photoluminescence measurements show that the spirals can enhance the forward emission of incoherent fluorescent sources embedded in a waveguide that also encloses the spiral. The enhancement occurs over a broad spectral band, proving the potential of Vogel's golden spirals for broadband light-emitting devices.

# Broadband light scattering and photoluminescence enhancement from plasmonic Vogel's golden spirals

**Ke Guo, Mengqi Du, Clara I. Osorio, and A. Femius Koenderink**

## 1. Introduction

The manipulation of light emission using optical antennas including accelerating spontaneous emission, redirecting usually omnidirectional fluorescence into narrow beams, and controlling polarization is an important topic of research for microscopy, spectroscopy and solid-state lighting. [1–12]. The plasmon resonances in optical antennas guarantees strong effects, albeit at the cost of Ohmic loss. In addition to single resonant antennas [1–8], one can use arrays of them [9–12], where the position of each antenna is an additional degree of freedom that can be tailored to achieve a desired functionality. In particular, periodic lattices of plasmonic nanoantennas are able to significantly enhance directional emission of nearby fluorophores [10–12]. However, periodic structures have two major drawbacks. First, the anisotropy of lattices hinders their use in applications that require cylindrically symmetric sources such as general lighting. Second, the use of diffractive resonances implies narrow bandwidth of enhancement (a few nm [11,12]), limiting the efficiency of the enhancement for most emitters such as quantum dots and organic dyes, which usually have large bandwidths at room temperature. These two drawbacks are results of the anisotropic and pure-point Fourier transform of periodic arrays. Therefore, for cylindrically symmetric and broadband manipulation of light emission, it is useful to arrange antenna array so that the Fourier transform is isotropic and broadband.

Deterministic quasi-periodic and aperiodic nanoantenna arrays with singular continuous or absolute continuous Fourier transforms [13] are considered a promising alternative design to overcome the limitations of periodic lattices [14–16]. Among these structures, plasmonic Vogel's golden spirals [17], like the one shown in Fig. 1(a), have been proposed as particularly interesting because they exhibit circularly symmetric and broadband light scattering features [16], as derived from the Fourier transform of the spiral array, shown in Fig 1(b). In this article, we study fluorescence enhancement from plasmonic Vogel's golden spirals. To this end, we first unravel the optical response of spirals using darkfield microscopy and k-space polarimetry [18–21]. We take into account the polarization response that is not available in Ref. [16], and investigate how far theoretical modeling should include antenna-antenna interactions. Next, we discuss studies on fluorescent samples where the spiral is embedded in an organic fluorescent waveguide layer. Directivity and spectra of fluorescence enhancement from the spirals are mapped using both Fourier imaging and Fourier spectral imaging techniques. We demonstrate that the investigated spirals can enhance the forward emission of incoherent sources in a waveguide over a very broad spectral band, which can be beneficial for cylindrically symmetric and broadband light-emitting devices.

## 2. Vogel's spiral

The Vogel's golden spiral shown in Fig. 1(a) consists of $N = 1000$ particles placed according to the generation rule

$$r = a\sqrt{n}, \qquad \theta = \theta_g \cdot n, \quad n = 1 \ldots N \tag{1}$$

where $(r, \theta)$ denotes the polar coordinates of the $n$th particle, and $\theta_g = 137.508°$ is the golden angle approximated by ratios of Fibonacci numbers, while $a$ is a constant scaling parameter [17]. This array has a quasi-isotropic particle distribution with inter-particle separation varying from $1.67a$ to $1.75a$. As a consequence, the Fourier transform of the array shown in Fig. 1(b) exhibits concentric double-ring structures near multiples of $0.59 \cdot 2\pi/a$ from the origin, with fine speckles. Meanwhile, the asymmetries in the array

Center for Nanophotonics, FOM Institute AMOLF, Science Park 104, 1098 XG Amsterdam, The Netherlands
* Corresponding author: emailf.koenderink@amolf.nl

result in a dense phase fluctuation in the phase of the Fourier transform. The finite thicknesses of the rings in the Fourier transform suggests broad spectral and angular bandwidths of the geometric scattering of spirals, much broader than would appear for periodic lattices that have a pure-point Fourier transform. It should be noted that for $\theta$ slightly away from $\theta_g$ one obtains handed spirals. In this paper we limit ourselves to golden spirals, while we have studied various pitches $a$, and particles numbers $N$.

In the limit that multiple scattering can be ignored, the Fourier transform of a structure is a first order approximation to its diffraction pattern upon illumination with a normal plane wave. Moreover, if the structure is a plasmon lattice embedded in a 2D fluorescent waveguide layer, a first approximation to the radiation pattern can be simply obtained from antenna theory [22]. The rationale is that emitters will dominantly emit into the waveguide mode, meaning that all emission will be characterized by having an in plane wave vector $\mathbf{k}_{||}$ of length $k_{\mathrm{WG}} = n_{\mathrm{WG}}\omega/c$ where $\omega$ is emission frequency, $c$ the speed of light and $n_{\mathrm{WG}}$ the mode index. The expected outcoupled light distribution can be constructed by considering how each in-plane wave vector $\mathbf{k}_{||}$ diffracts, followed by summation over all excited wave vectors. Mathematically, in the limit of single scattering, this means that one obtains the radiation pattern by convoluting the spiral Fourier transform with the wave vector distribution of emission, which is a circle in k-space of radius $k_{\mathrm{WG}}$ [23, 24]. As illustrated in Fig. 1(c), when the propagation constant of the waveguide mode ($k_{\mathrm{WG}}$) exactly matches the radius $k_{\mathscr{F}}$ of the first ring in the Fourier transform of the structure, the scattering of the array shifts the waveguide modes by $k_{\mathscr{F}}$ in all directions, resulting in an overlap of the outcoupled waveguide modes at the origin. This intuitive picture suggests emission enhancement from the spiral array will appear in the forward direction for appropriately chosen size parameter. However, this qualitative analysis does not take into account three factors that may have an significant influence on the emission enhancement. First, coupling between individual antennas can affect the scattering pattern of the array making the Fourier transform an inaccurate prediction. Second, the sketch in Fig. 1(c) does not contain the phase variations in Fig. 1(b), indicating that interference effects could require further analysis. Finally, an actual device contains an ensemble of incoherent emitters at different positions relative to the array. The incoherent average of emission from all emitter positions could result in an emission pattern significantly different from emission patterns that individual sources give. In what follows, we study plasmonic Vogel's golden spirals to take into account these three factors.

## 3. Scattering

In this section, we study the light scattering properties of Vogel's golden spirals of gold nanoantennas using dark-field microscopy and k-space polarimetry. The spirals are fabricated on silica substrates ($n = 1.51$) using electron beam lithography (20 kV, ZEP-resist), thermal evaporation of Au, and subsequent liftoff. The resulting nanoantennas have a cylindrical shape and a height of 30 nm. The sample geometries that we explore include various antenna size, effective pitch parameter $a$, and particle number $N$.

We perform dark-field microscopy using a reflection-configuration. A halogen lamp is focused by either a 50× dark field objective with NA = 0.8 or a 20× dark field objective with NA = 0.45, illuminating the samples through the substrate. The same objective collects the back-scattered light and sends it to a 70/30 beam splitter. A fraction of 70% of the scattered light is transmitted and imaged on a camera (Image Source DFK 21AU04). The remaining 30% is reflected to a multi-mode fiber with a core of 400μm and NA = 0.39, which is connected to a spectrometer (Avaspec 2048TEC-2-USB2) with a detection wavelength range of 500 to 1000 nm. Fig. 2 shows dark-field images of spirals composed by 55 nm radius antennas with $a = 300$, 250 and 200 nm, taken with the 50× objective (a-c) and the 20× objective (e-g) on the camera (identical, fixed white balance for all images). The qualitative color variations observable in the images are confirmed by the scattering spectra in Fig. 2(d) and (h). For $a = 300$ nm, individual antennas can be resolved by the 50× objective, which appear as orange diffraction-limited spots, reflecting a localized resonance of individual antennas at $\lambda \approx 600$ nm. As $a$ decreases, the spiral structure becomes unresolvable due to the diffraction limit and, furthermore, the color appearance of the spirals becomes distinctly different. In particular, we observe three phenomena. First, we note that the color appearance of the spirals depends on the location within the spiral. Second, as the pitch $a$ is reduced, the color impression strongly varies giving rise, for instance, to deep blue for $a = 250$ nm in panel (f) and purple (a combination of blue and red) in panel (g). Third, the color impression strongly depends on the numerical aperture of the microscope objectives.

Two possible explanations for these phenomena are that dipole-dipole coupling between antennas causes resonances to shift, in the vein of plasmon hybridization [25, 26], or that diffraction by clusters of the antennas that make up the spiral is angle dependent, resulting in a difference in the collection efficiency of scattered light depending on color and pitch. Since in these systems the particle spacing is comparatively large (mean nearest neighbor distance is $\sim 1.7a$), and plasmon hybridization would not give a strong angle dependence, the dominant effect is diffraction, not shifting of resonances due to hybridization. The strong dependence of color appearance on the numerical aperture of the objective corroborates this interpretation. Since illumination is through the objective mantle, the sample is illuminated by only a narrow cone of incident angles. Color appearance depends on whether this narrow cone is diffracted into or away from the objective collection lens. For instance, the apparent absence of the plasmon feature in the NA=0.45 spectrum at $a = 250$ nm and concomitant blue camera appearance is commensurate with the fact that the strong scattering at the plasmon resonances is diffracted into large angles outside the detection cone.

Additional evidence for the conclusion that diffraction is determining for appearance is provided by two further obser-

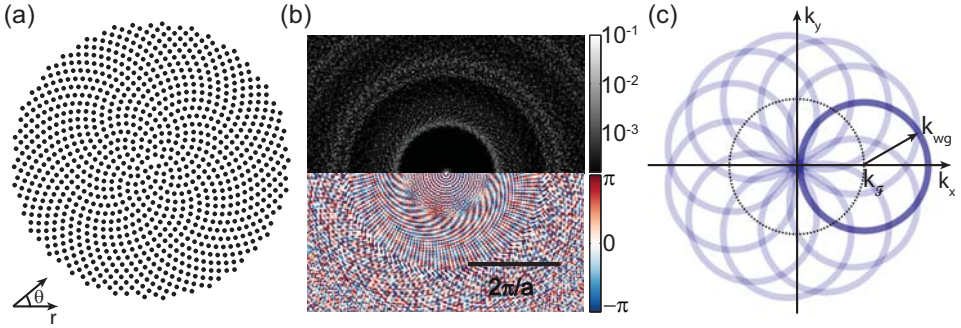


**Figure 1** (a) A Vogel's golden spiral composed by 1000 elements. (b) The absolute value (top, normalized) and phase (bottom) of the Fourier transform of (a). (c) An illustration of the distribution of waveguide modes outcoupled by a Vogel's golden spiral.

vations. On the one hand, data taken from bigger antennas with identical pitch show similar coloration, albeit that the dark field intensity is increased (Fig. s1 in supplementary). Since diffraction mainly depends on particle spacing while hybridization would depend on particle size, this observation points at diffraction. On the other hand, the notion that diffraction given by the local nearest-neighbor distance, or local cluster geometry, determines appearance is evidenced by the strong correlation of color appearance with nearest neighbor distance. The inset in panel 2(c) shows the nearest-neighbor distance as a function of the distance to the spiral center. Small variations of around 15 nm around the mean ($< 5\%$ variations around 340 nm for the $a = 200$ nm spiral) correlate directly with the subtle changes in color appearance. We have also studied color appearance in spirals that are not the golden spiral, but instead have $\theta = n(\theta_g \pm \Delta\theta)$ with $\Delta\theta$ in the order of $0.1°$, as shown in Fig. s2 of supplementary information. The resulting spirals are not only handed, but also have more distinct density variations in the radial direction, as opposed to the quite uniform golden spiral. These non-golden spirals show distinct color variations that correlate with local particle density.

Having established that golden spirals show strong diffraction colors, we perform Fourier microscopy to measure the angle-dependent diffraction patterns at normal incidence. For this study we choose antennas with 95 nm radius for strong scattering intensity, and vary the particle number $N$, the pitch parameter $a$ and the wavelength $\lambda$. Figure 3 (a) shows a schematic of the setup, which is similar to that used in Ref. [21, 27]. A super-continuum laser that is weakly focused by a $10\times$ objective illuminates the sample from the air side in the normal direction, with the output wavelength selected by an acousto-optic tunable filter (AOTF). A $100\times$ oil immersion objective with a NA $= 1.4$ collects the scattering from the side of the substrate and sends it through a telescope. In the center of the telescope, where the sample is imaged with a magnification of $25\times$, a 200μm pin-hole is used to select light from the central part of the spiral and block the light transmitted from the surrounding substrate. Behind the telescope, a Fourier lens and a tube lens are used to image the back-focal plane of the objective onto a CCD camera with $1\times$ magnification. The Fourier image of the scattering is dominated by the zero-order transmittance which results in a bright spot in the center of the Fourier image in addition to a much weaker ring of diffracted light. To suppress the zero-order transmittance, we place a disk-shaped beam block with a diameter of $\sim 500$ μm in the center of the back focal plane, leaving a detection range of $0.18k_0 < |k| < 1.4k_0$. Figure 3(b) shows a back focal plane image of a spiral with $a = 300$ nm, illuminated with a vacuum wavelength of $\lambda = 600$ nm. The image presents low intensity for low k ($0.18k_0 < |k| < k_0$), surrounded by a distinct bright ring at $|k| \approx 1.1k_0$, corresponding to diffraction at angles around $46°$ off the sample normal into the glass substrate. The position of the ring corresponds well to the Fourier transform in Fig. 1. We verify that the radius in k-space of the ring scales as expected with pitch $a$ and wavelength $\lambda$, meaning that it remains at the same $|k|/k_0 = 0.59\lambda/a$ independent of the dimensionless ratio $a/\lambda$, while scaling with both independently, shown in Fig 3(b-d). As is the case in the calculated structure factor (Fig. 1(b)), the scattering ring has a speckled appearance. For a fix set of $a$ and $\lambda$, the size of the speckle size is coarsest for least number of particles, reducing with increasing $N$ from 200 to 1000, as shown in Fig 3(e-g). This agrees with the fact that, in general, the size of speckles or diffraction features generated from a radiating object in the Fourier plane is inversely proportional to its size.

Dark field and Fourier microscopy measurements suggest that the spirals are diffractive structures that consist of essentially uncoupled scatterers. For further confirmation, we perform k-space polarimetry [18–21]. Two polarimeters, placed respectively before and after the sample, select the polarization of the illumination and detection. We obtain the Stokes parameters ($S_0$, $S_1$, $S_2$, $S_3$) of the Fourier images of the scattering by fixing the illumination polarization and doing six measurements with different polarimeter settings in the detection path. Detailed polarimeter settings can be found in the supplementary information. Figure 4(a-b) show the Stokes parameters for linearly and circularly polarized excitation. As shown in Fig. 4(a), for horizontally polarized input, the total scattering intensity from the spiral ($S_0$) resembles its Fourier transform, presenting a distinct, speckled, circular band. In addition, as a factor apparently multiplying the Fourier transform, the intensity is high at small $k_x$ and low at large $k_x$. This asymmetry rotates with the incident

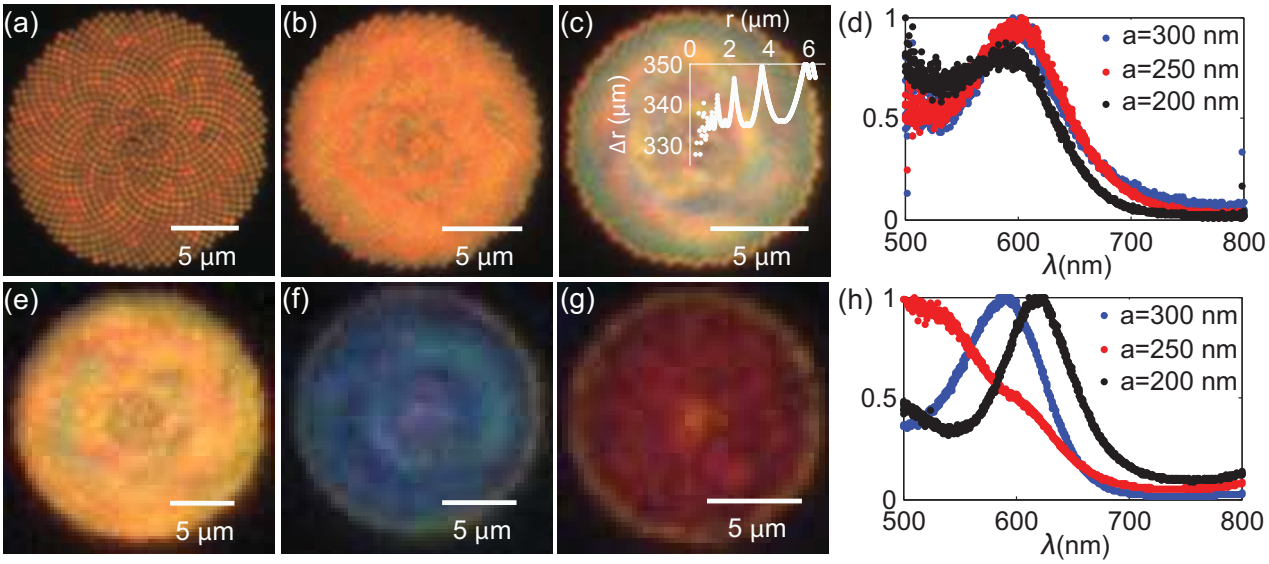


**Figure 2** Dark field images of spirals with (a)(e) $a = 300$ nm, (b)(f) 250 nm and (c)(g) 200 nm and dark field scattering spectra measured with (a-d) a 50× objective and (e-h) a 20× objective. (c) is over-plotted with the nearest-neighbor distance for each nanoantenna as a function of its distance to the center.

polarization, and indicates that the scattering is essentially the product of the structure factor of the array, and the emission pattern of a linearly polarized dipole oriented along the incident polarization [24,27]. At positions where the total intensity $S_0$ is low, $S_1/S_0$, $S_2/S_0$ and $S_3/S_0$ have random values. For most of the positions in the Fourier space where $S_0$ is above the noise, $S_1/S_0$ is close to 1 and both $|S_2/S_1|$ and $|S_3/S_1|$ are low, meaning that the polarization of the scattered light has been mostly preserved. However, near $|k_x| = |k_y|$, $|k| = k_0$ where the image diagonals intersect the $NA = 1$ circle, $|S_1/S_0| \approx 0$ and $|S_2/S_0| \approx 1$ indicating a rotation of the polarization by $\sim 45°$. Just outside the NA $= 1$ circle and at $|k_x| = |k_y|$ both $|S_1/S_0|$ and $|S_2/S_0|$ are low and $|S_3/S_0| \approx 1$, indicating that circularly polarized light has been generated despite the linear driving polarization. For circular input polarization (Fig. 4(b)), the scattered light shows a scattering pattern that is rotationally symmetric ($S_0$), with essentially circular polarization identical to the input field for $|k| < k_0$, and conversion to linear polarization at $|k| > k_0$. Thanks to the circular symmetry of the spiral, the Stokes parameters associated to linear polarization, $S_2$ and $S_1$, are equal to each other but rotated by 45°. We have verified that these features remain unchanged when varying $a$, barring the expected scaling of the diffraction ring with $a$.

To answer the question whether the antenna-antenna interactions have a significant influence on the scattering pattern of the spiral, we model the sample as an array of point dipoles 15 nm (half the particle thickness) above a substrate. When multiple scattering is weak and the coupling between the antennas is negligible, the radiation pattern is essentially the coherent superposition of the radiation from many identically aligned induced dipoles, which have a dipole polarization inherited from the incident field polarization. Under this assumption, we calculate the scattering intensity $S_0$ as the product of the array structure factor, i.e., the Fourier transform, and the single dipole radiation pattern (acting as form factor). $S_1/S_0$, $S_2/S_0$, $S_3/S_0$ are calculated from a single point dipole in the x direction on a substrate [28,29]. Fig. 4(c) shows the calculated Stokes parameters of the radiation from a spiral array of uncoupled point dipoles with equal dipole moment in the horizontal direction, which have the same distribution for the intensity and polarization of scattering that we measured, shown in Fig. 4(a). This implies that the response of the investigated spiral to the incident field can indeed be described as a group of uncoupled dipoles. Notice that for $k \geq 1$, the change of polarization results from the air-substrate interface instead of the spiral arrangement. The radiation pattern of a dipole above a substrate incorporates the Fresnel-coefficient of the interface. The difference in amplitude of the transmission coefficients for TM and TE polarizations rotates the polarization and the difference in phase generates circular polarization. Similar agreement between measurement and a model of uncoupled dipoles that inherit there dipole moment from the drive polarization has been found with left-hand circularly polarized input as shown in Fig. 4(d). The conversion of circular polarization to linear polarization at $|k| > k_0$ is also a result of the difference in transmission coefficients. The spiral arrangement only determines the scattering intensity ($S_0$) distribution and has no influence on the polarization of scattered light ($S_1/S_0$, $S_2/S_0$, $S_3/S_0$).

## 4. Photoluminescence enhancement

In this section, we investigate the photoluminescence (PL) enhancement of the Vogel's spirals. A 600 nm polystyrene layer ($n = 1.6$ at $\lambda = 600$ nm) doped with 3 wt. % dye molecules (Lumogen Red F305 (BASF)) was spin-coated

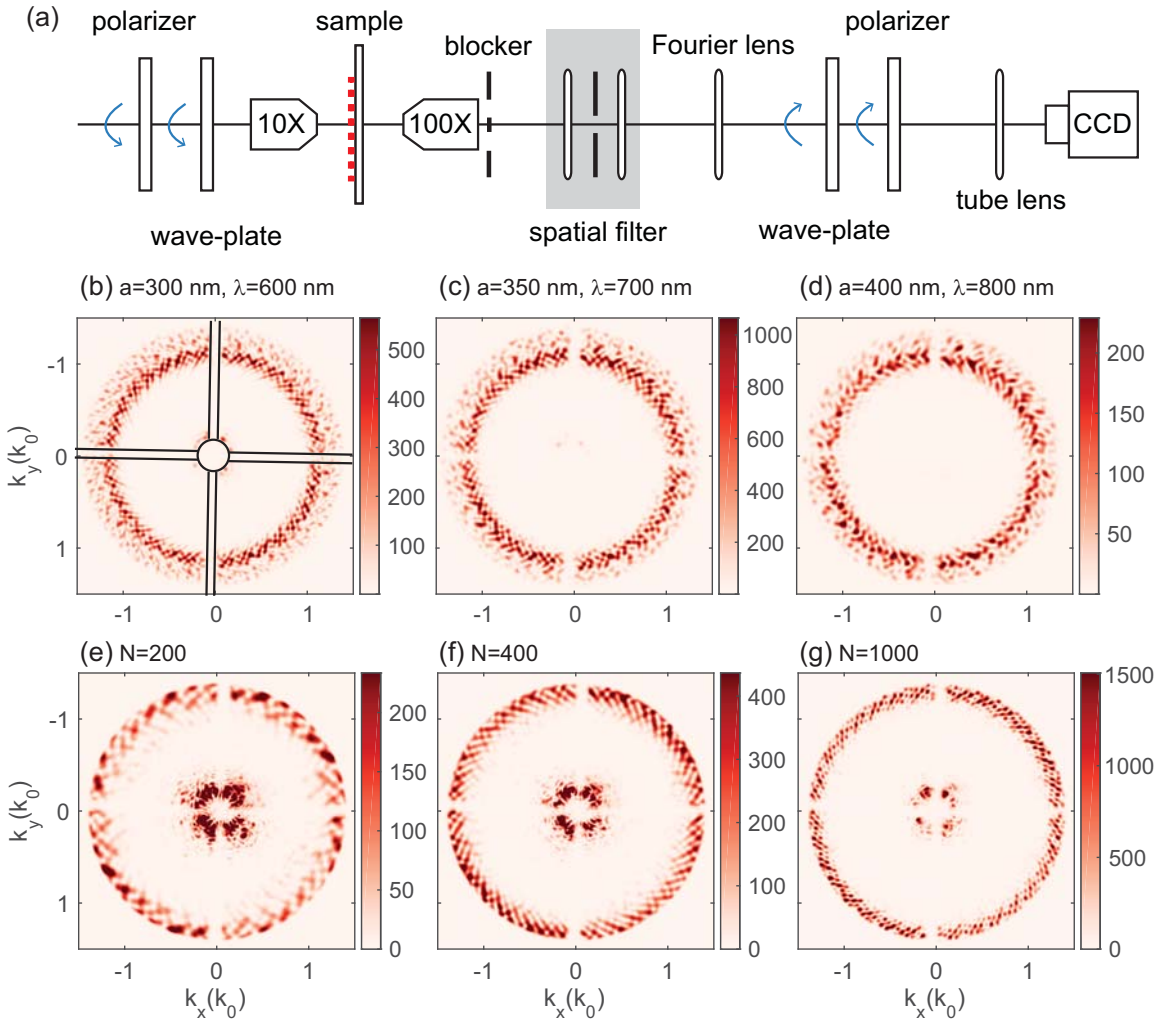


**Figure 3** (a) A schematic of the setup for Fourier polarimetry measurement. (b-d) Back focal plane images of light scattering from spirals with a fix ratio $a/\lambda = 0.5$ and $N = 1000$. (b)$a = 300$ nm, (c) 350 nm and (d) 400 nm. (e-g) Back focal plane images of light scattering from spirals with $a = 200$ nm, $\lambda = 490$ nm and different $N$. (e) $N = 200$, (f) 400 and (g) 1000. Black lines in (b) illustrate the shape and position of the beam block.

on the sample, resulting in a waveguide with fundamental TE- and TM-modes with effective refractive index of $n_{WG} \sim 1.58$ in the visible (numbers from mode calculation [30]). The dye molecules have an absorption spectrum in the green (maximum absorption near 560 nm) and an emission spectrum in the red (620 nm). The geometry of a waveguide layer with this dye was chosen because it has been shown to be very effective for directional photoluminescence enhancements when used in conjunction with periodic plasmon particle arrays [11]. In order to outcouple the waveguide modes into the forward direction, we choose $a$ to be around 225 nm, as for this pitch the first ring in the Fourier transform occurs at $1.58k_0$ for the emission wavelength, which overlaps with the waveguide modes in k-space, commensurate with the directional out-coupling criterion constructed in Fig.1(c).

We performed Fourier-plane microscopy on the PL using the same setup as in the scattering measurements but without polarimeters. The sample was excited with wavelength of 550 nm and the emission wavelengths was selected with a 10 nm bandpass filter at 620 nm. Figure 5(a) shows the Fourier image of PL from a dye layer on a bare substrate used as reference. The Fourier image appears as a disk with a size determined by the NA of the objective and high intensity at $1 < |k| <$ NA, which agrees with the emission pattern expected from an ensemble of randomly oriented dipoles in a waveguide [29]. Figure 5(b) shows the Fourier image of PL from the dye layer on the spiral with $a = 225$ nm and Fig. 5(c) shows a comparison between the PL from the spiral sample and the reference in an image slice taken at $k_y = 0$. The emission in the forward direction is significantly enhanced due to out-coupling of the waveguide modes through diffraction by the spiral. We calculate the PL enhancement (PLE) by dividing the spiral-enhanced PL by the reference PL. Figure 6 shows the measured PLE of spirals with $a = 200$, 225, 250 and 275 nm. All the spi-

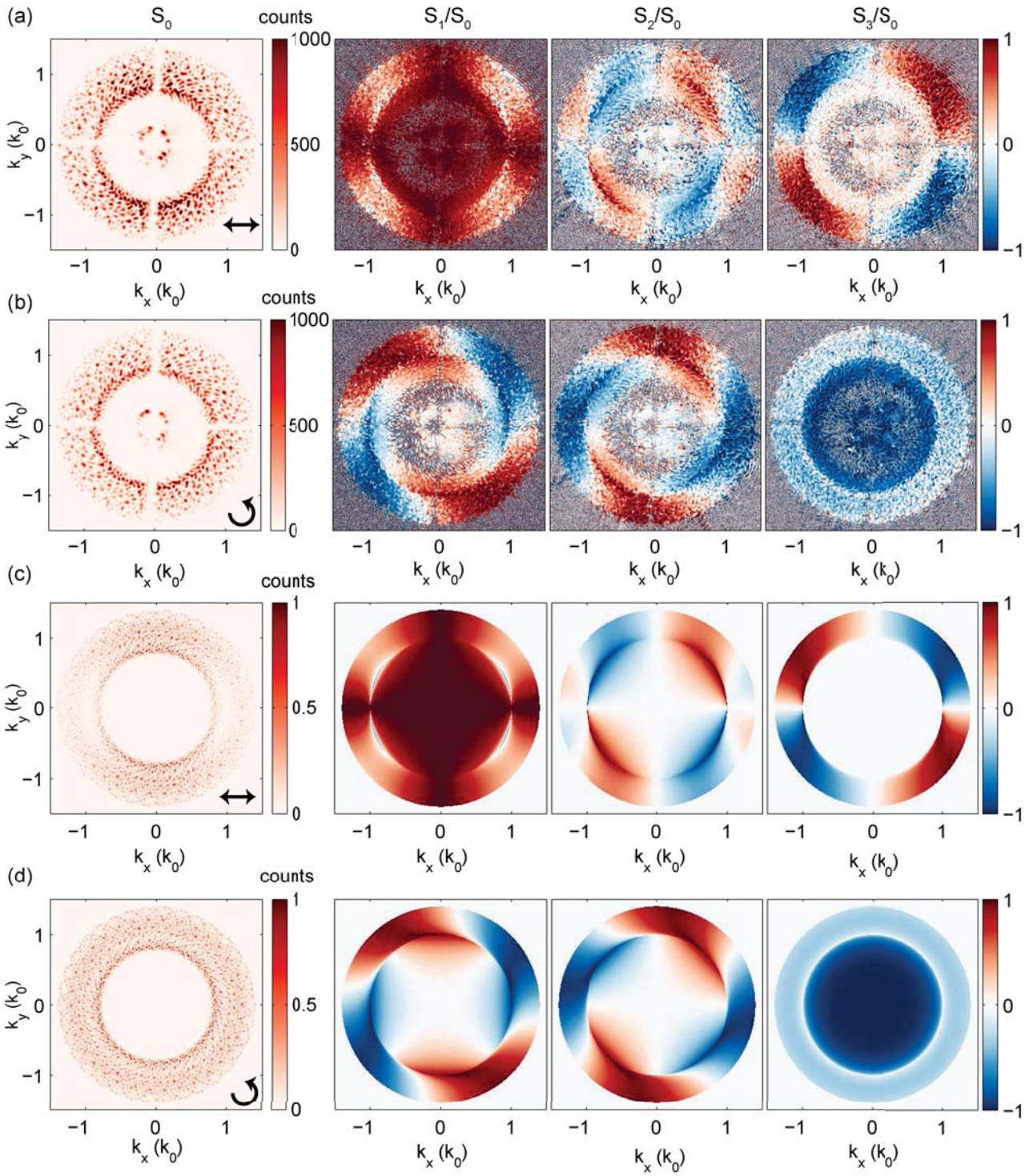


**Figure 4** Measured (a-b) and calculated (c-d) Stokes parameters of the scattered light from the spiral with (a) and (b) horizontally and (c) and (d) left-handed circularly polarized input. $a = 400$ nm, $N = 1000$.

rals show circularly symmetric PLE at small $|\boldsymbol{k}|$, with PLE enhancement values from 1.5 to 2. With increasing $a$, the enhancement shifts from being a ring $|\boldsymbol{k}| \approx 0.2k_0$ (8° in the glass) to a central maximum at $|\boldsymbol{k}| = 0$ and increases until it is maximized in the forward direction with $a = 225$ nm. For $a = 250$ nm, the enhancement decreases and furthermore reverts to being a ring at $|\boldsymbol{k}| \approx 0.3k_0$ (11° in the glass). Stokes parameter polarimetry measurements of the output show that the enhanced fluorescence intensity is entirely unpolarized, as might be naively expected from a random

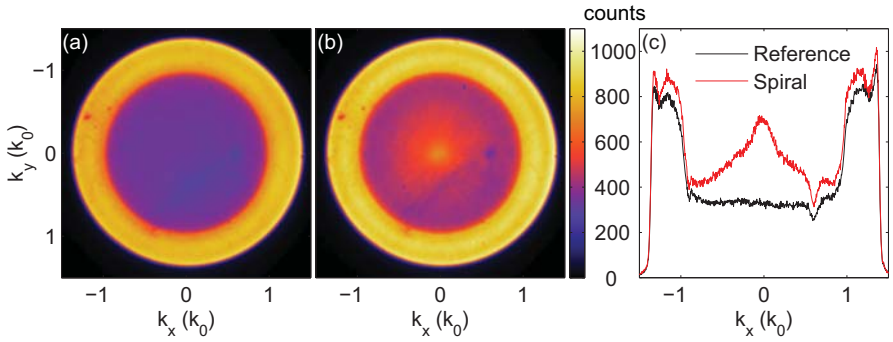


**Figure 5** Measured Fourier images of fluorescence at $\lambda$=620 nm from (a) the reference, which is a 600 nm dye layer (b) and the same dye layer on the spiral. $a = 225$ nm, $N = 1000$. (c) Cuts from (a) and (b) at $k_y = 0$, plotted with the same scale of the colorbar.

ensemble of emitters and a plasmonic structure with no preferential orientation [31]. This is a remarkable difference of the investigated spiral arrays from periodic arrays, from which the diffractive surface lattice resonances can carry a strong polarization signature [32].

We model the dispersion of the enhancement by assuming the nanoantenna array as a group of identical uncoupled point dipoles that coherently radiate into the far field, after having been driven by a point source that isotropically excites the waveguide mode supported by the dye layer, and that mimics a fluorophore. According to radio wave antenna theory, if the induced dipole moment of an antenna at location $\boldsymbol{r}$ is $p = \alpha E_D(\boldsymbol{r})$, with local driving field $E_D(\boldsymbol{r})$ and scalar polarizability of each nanoantenna $\alpha$, the radiation pattern follows by summation over all antennas

$$E(\mathbf{k}_{||}) \propto \sum_{n\in\text{spiral}} E_D(\boldsymbol{r}_n)\alpha e^{-\mathrm{i}\boldsymbol{k}_{||}\cdot\boldsymbol{r}_n}$$
$$\propto \alpha \int_{\text{plane}} E_D(\mathbf{r}) \cdot \sum_{n\in\text{spiral}} \delta(\mathbf{r}-\mathbf{r}_n) e^{-\mathrm{i}\boldsymbol{k}_{||}\cdot\boldsymbol{r}}, \qquad (2)$$

with $\boldsymbol{r}_n$ the position of each nanoantenna. In this expression a common prefactor that is a spherical wave has been suppressed. Using the convolution theorem, the far field distribution is the convolution of the driving field $E_D$ transformed to k-space, and the Fourier transform ($\mathscr{F}$) of the spiral structure, i.e.

$$E(\boldsymbol{k}_{||}) \propto \mathscr{F}[E_D] \star \mathscr{F}[\sum_{n\in\text{spiral}} \delta(\boldsymbol{r}_n)]. \qquad (3)$$

In our sample, the driving field is dominated by the waveguide modes generated by the fluorescence of randomly distributed incoherent dye molecules. For an emitter located at the origin that predominantly emitted into the waveguide mode, the driving field in k-space simply is a circle with radius given by the waveguide mode index. More formally stated, it is approximated as the Fourier space representation of the 2D Green function of the Helmholtz equation, i.e., $|\boldsymbol{k}^2 - n_{WG}^2 k_0^2|^{-1}$, with $n_{WG}$ the mode index. The emitted power ($P_{\boldsymbol{k}} = |E_{\boldsymbol{k}}|^2$) as calculated from the convolution is expected to be a speckled ring at large wave vector and low intensity at the origin as shown in Fig. 6(e-h). In earlier work on periodic plasmon array systems it has been reported that the radiation pattern of a single emitter in the unit cell already predicts very well the radiation pattern of an incoherent ensemble [23]. Instead, here we see a striking difference between the measured ensemble-averaged pattern, and the distribution of emission that one would expect for just a single source at the origin. This contradiction indicates that (i) the dense fluctuation in the phase of the Fourier transform has a significant influence and (ii) likely, emitters in different positions result in a very different emission pattern in terms of amplitude and phase. Indeed, the predictions in Fig. 6(e-h) show angularly narrow speckle, and destructive interference that suppresses the forward emission, while for other source positions we predict quite different patterns. Therefore, to make a more accurate prediction, we need to consider an incoherent sum of contributions from random source positions.

The Fourier shift theorem states that a shift in position by $\boldsymbol{r}_D$ of the driving source only results in a phase shift of the Fourier transform of the driving field [23] as:

$$\mathscr{F}[E_D(\boldsymbol{r}_D)] = e^{\mathrm{i}\boldsymbol{k}_{||}\cdot\boldsymbol{r}_D}\mathscr{F}[E_D(0)]. \qquad (4)$$

Thus, the total emission power from an ensemble of randomly distributed incoherent source can be calculated as:

$$P_{\boldsymbol{k}_{||}} \propto \int \mathrm{d}\boldsymbol{r}_D \left| e^{\mathrm{i}\boldsymbol{k}_{||}\cdot\boldsymbol{r}_D}\mathscr{F}[E_D(0)] \star \mathscr{F}[\sum_{n\in\text{spiral}} \delta(\boldsymbol{r}_n)] \right|^2. \qquad (5)$$

By expanding $|.|^2$ as a product, writing out the convolution integrals and then switching the order of integration, we can simplify the above formula to

$$P_{\boldsymbol{k}} \propto |\mathscr{F}[E_D(0)]|^2 \star |\mathscr{F}[\sum_{n\in\text{spiral}} \delta(\boldsymbol{r}_n)]|^2. \qquad (6)$$

This is a generally useful and remarkable result for periodic and non-periodic plasmonic array structures aimed at controlling the directivity of random uniformly distributed ensembles of incoherent emitters. It states that, while the radiation pattern of a single emitter is given by the k-space convolution of the single emitter field and the complex structure factor, the radiation pattern of the incoherent ensemble

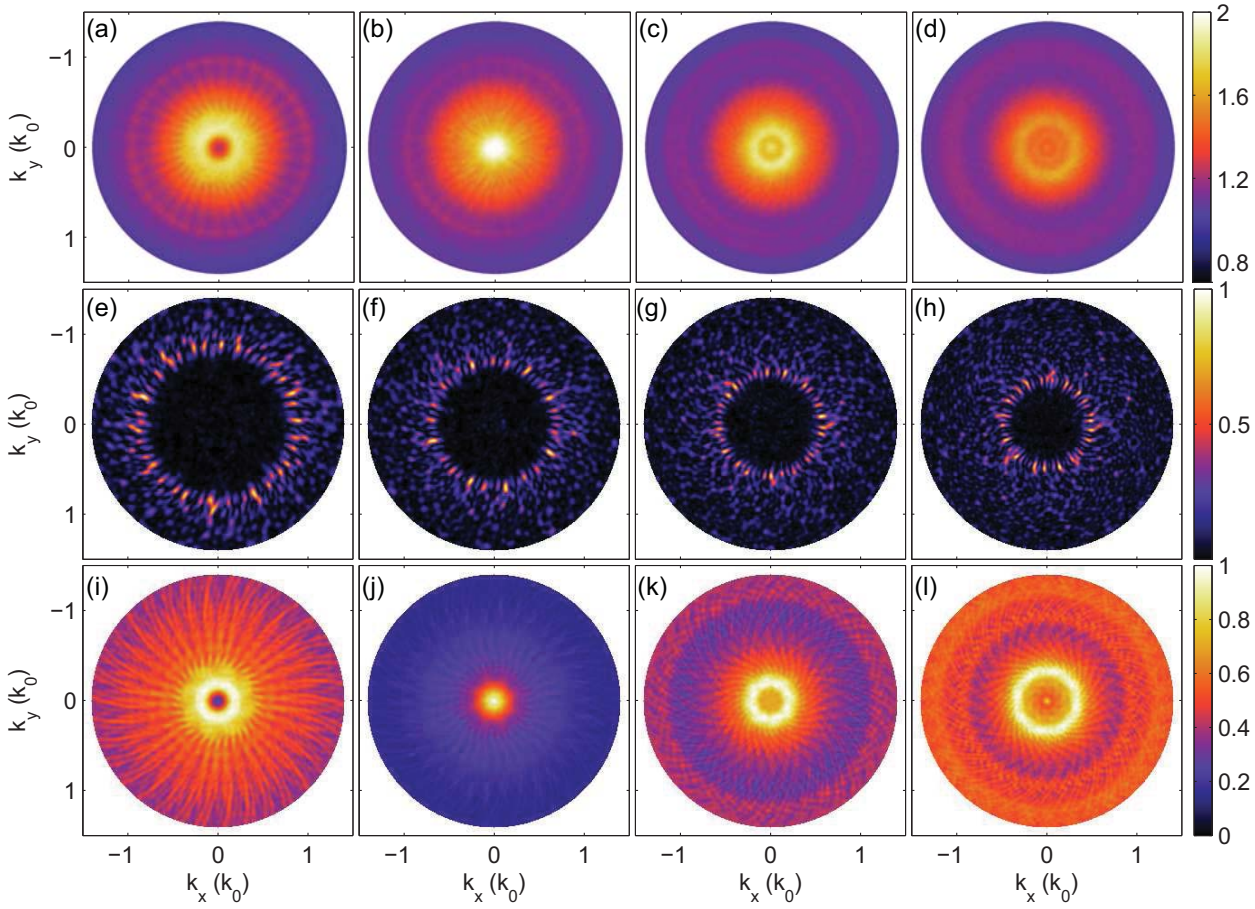


**Figure 6** Fourier images of PLE on a 600 nm dye layer from spirals. (a-d) are measurement results. (e-h) are calculated from Eq. 3 and (i-l) are calculated from Eq. 6. (a)(e)(i) $a = 200$ nm, (b)(f)(j) 225 nm, (c)(g)(k) 250 nm, (d)(h)(l) 275 nm. (e-h) are normalized to the maximum of (f). (i-l) are normalized to the maximum of (j). $N = 1000$.

is the k-space convolution of the single emitter intensity and the absolute value squared of the structure factor. Practically, this means that the rapid phase fluctuations in Fig. 1(b) simply average out. Fig. 6 (i-l) show the calculated emission patterns for the four measured spirals assuming such incoherent averaging. We find excellent agreement with the measurements in terms of enhancement position and relative strength. We conclude that, while spirals are not very suited for beam shaping of single emitters because of their tendency to imprint a rapidly fluctuating amplitude and phase pattern, in fact on the ensemble level the investigated spirals are able to out-couple ensemble emission in a phosphor layer in a directional manner.

Finally we study the bandwidth of the enhancement. We measure the Fourier spectra of the four spirals using the setup of Ref. [33]. The spirals are excited from the substrate side through a 100×/ 1.45NA objective using a 532 nm microchip laser (Teem Photonics, type STG-03E-1S0). The laser is focused near the backfocal plane of the objective and an iris is used to ensure that the whole spiral, but no region around it, is illuminated. The emission is collected by the same objective. After removing laser light by a longpass filter (cut-off at 550 nm), the backfocal plane of the objective is imaged on the entrance plane of a Shamrock 303i spectrometer with an iDus CCD camera. The slit of the spectrometer is placed at the center of the Fourier image to select the emission near $k_x = 0$. Using the spectrometer CCD in imaging mode, we are thus able to obtain a spectrally resolved Fourier image, with emission intensity as a function of $k_y$ and $\lambda$. Dividing the Fourier spectra images from the dye layer on spirals by the images from the reference, we obtain the PLE. Figures 7(a-f) show PLE for samples with 6 different pitches, plotted as function of dimensionless parameter $k_y \cdot a$ and dimensionless frequency $\omega a/2\pi c = a/\lambda$. Under the condition of negligible dispersion in the waveguide index, one would expect this scaling to align the diffractive features in all samples. Indeed, according to Eq. 5, the PLE has approximately the same dependence on $\boldsymbol{k}$ and $a/\lambda$ for all the four spirals. The maximum value of enhancement is slightly below that in Fig. 6, which we attribute to a difference in pump wavelength and angle. Nevertheless, the dispersion of the enhancement agrees well. The enhancement is maximized at $k_y \cdot a = 0$ and $a/\lambda \approx 0.36$ ($a = 225$ nm for $\lambda = 620$ nm) and then shifts to larger $k_y \cdot a$ as $a/\lambda$

continues increasing. At $a/\lambda \approx 0.36$ the photoluminescence at small angle is suppressed.

With the same model used for Fig. 6(i-l), we obtain the theoretical dispersion of PLE in Fig. 7(g), which again agrees with the measurement result in terms of both the position of the enhancement and the relative strength of the enhancement. Both the experiment and theory show a broadband enhancement near the forward direction over $a/\lambda = 0.34$ to 0.38, corresponding to a bandwidth of around 60 nm for $a \approx 200$ nm, much larger than the bandwidth reported for periodic structures. This bandwidth makes spirals suitable for enhanced directional emission of many promising light-emitting devices that use quantum dots [34–37] and organic dyes for conversion to white light. These fluorophores have a typical bandwidth of $30-100$ nm at room temperature.

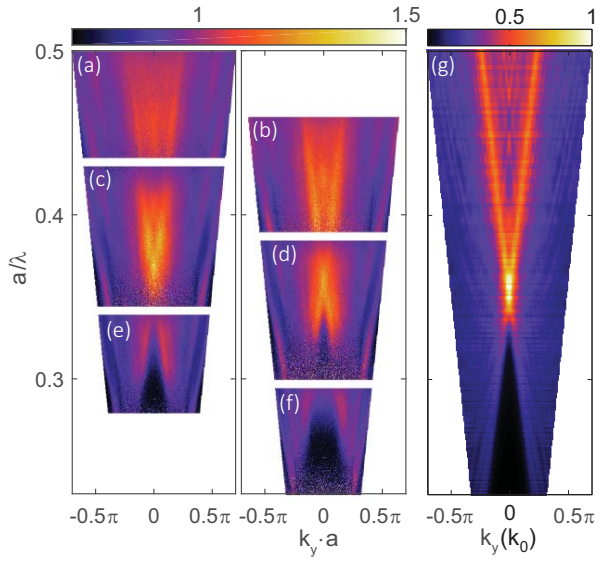


**Figure 7** Measured Fourier spectra of Fluorescence enhancement on the 600 nm dye layer from spirals with (a) $a = 300$ nm (b) 275 nm, (c) 250 nm, (d) 225 nm, (e) 200 nm and (f) 175 nm, $N = 1000$. (e) Emission enhancement predicted from Eq. 6 normalized to the maximum.

## 5. Conclusion

We have fabricated Au nano-antenna arrays arranged as Vogel's golden spirals and characterized their scattering properties using dark field microscopy and k-space polarimetry microscopy. The dark field images reveal a localized surface plasmon resonance near 600 nm for individual nanoantennas in the spirals, yet strong diffractive coloring for spirals with $a < 300$ nm. Comparing Fourier-space polarimetry results with a theoretical model, we have furthermore concluded that the investigated spirals ($a = 400$ nm) react to the incident field as uncoupled dipole arrays, meaning that one obtains scattering pattern determined by the spiral Fourier transform, and polarization characteristics inherited from that of single dipole scatterers at the air-substrate interface. Finally we have measured and modeled the directional fluorescence enhancement from the spirals. We demonstrate that the spirals can enhance the forward emission from incoherent sources in a waveguide by out-coupling the waveguide modes. While modest in magnitude, the enhancement spans over a wide spectral band of around 60 nm and therefore can be useful for emitters with a relevant bandwidth. The strength of the enhancement, can be boosted through the design of each of the nanoantennas. For example, optimizing the shape, size and material of the nanoantennas can increase the scattering strength and therefore further enhance the out-coupling. We further note that the enhancement is only dependent on the amplitude of the Fourier transform and not the phase. Therefore, similar ideas could be pursued in other structures with similar strongly banded rotationally symmetric structure factors, such as hyperuniform lattices. [38, 39]

**Acknowledgements.** This work is part of the research program of the "Foundation for Fundamental Research on Matter (FOM)", which is financially supported by the "The Netherlands Organization for Scientific Research (NWO)". A.F.K. gratefully acknowledges an NWO-Vidi and Vici grant for financial support.

**Key words:** plasmonic antennas, spontaneous emission, Vogel's spiral

## References

[1] A. Kinkhabwala, Z. Yu, S. Fan, Y. Avlasevich, K. Mullen, and M. E., Nat Photon **3**(11), 654–657 (2009).
[2] S. Kühn, U. Håkanson, L. Rogobete, and V. Sandoghdar, Phys. Rev. Lett. **97**(Jul), 017402 (2006).
[3] H. Mertens, A. F. Koenderink, and A. Polman, Phys. Rev. B **76**, 115123 (2007).
[4] P. Anger, P. Bharadwaj, and L. Novotny, Phys. Rev. Lett. **96**, 113002 (2006).
[5] R. J. Moerland, T. H. Taminiau, L. Novotny, N. F. van Hulst, and L. Kuipers, Nano Lett. **8**, 606–610 (2008).
[6] H. Gersen, M. F. García-Parajó, L. Novotny, J. A. Veerman, L. Kuipers, and N. F. van Hulst, Phys. Rev. Lett. **85**(Dec), 5312–5315 (2000).
[7] P. Mühlschlegel, H. J. Eisler, O. J. F. Martin, B. Hecht, and D. W. Pohl, Science **308**(5728), 1607–1609 (2005).
[8] T. H. Taminiau., F. D. Stefani, F. B. Segerink, and N. F. van Hulst, Nat Photon **2**(4), 234–237 (2008).
[9] A. G. Curto, G. Volpe, T. H. Taminiau, M. P. Kreuzer, R. Quidant, and N. F. van Hulst, Science **329**(5994), 930–933 (2010).
[10] K. H. Cho, J. Y. Kim, D. G. Choi, K. J. Lee, J. H. Choi, and K. C. Choi, Opt. Lett. **37**(5), 761–763 (2012).
[11] G. Lozano, D. J. Louwers, S. R. Rodriguez, S. Murai, O. T. Jansen, M. A. Verschuuren, and J. Gómez Rivas, Light Sci Appl **2**(May), e66 (2013).
[12] G. Lozano, G. Grzela, M. A. Verschuuren, M. Ramezani, and J. Gómez Rivas, Nanoscale **6**, 9223–9229 (2014).
[13] L. Dal Negro and S. Boriskina, Laser & Photonics Rev. **6**(2), 178–218 (2012).
[14] R. Dallapiccola, A. Gopinath, F. Stellacci, and L. D. Negro, Opt. Express **16**(8), 5544–5555 (2008).

[15] C. Forestiere, G. Miano, G. Rubinacci, and L. Dal Negro, Phys. Rev. B **79**(Feb), 085404 (2009).
[16] J. Trevino, H. Cao, and L. D. Negro, Nano Lett. **11**(5), 2008–2016 (2011), PMID: 21466155.
[17] H. Vogel, Mathematical Biosciences **44**(3), 179 – 189 (1979).
[18] C. Fallet, T. Novikova, M. Foldyna, S. Manhas, B. H. Ibrahim, A. De Martino, C. Vannuffel, and C. Constancias, Journal of Micro/Nanolithography, MEMS, and MOEMS **10**(3), 033017–033017–7 (2011).
[19] O. Arteaga, B. M. Maoz, S. Nichols, G. Markovich, and B. Kahr, Opt. Express **22**(11), 13719–13732 (2014).
[20] S. S. Kruk, M. Decker, I. Staude, S. Schlecht, M. Greppmair, D. N. Neshev, and Y. S. Kivshar, ACS Photonics **1**(11), 1218–1223 (2014).
[21] C. I. Osorio, A. Mohtashami, and A. F. Koenderink, Sci. Rep. **5**(9966) (2015), Article.
[22] C. A. Balanis, Antenna Theory: Analysis and Design, 3rd edition (Wiley, 2012).
[23] L. Langguth, A. H. Schokker, K. Guo, and A. F. Koenderink, Phys. Rev. B **92**(Nov), 205401 (2015).
[24] L. Langguth, D. Punj, J. Wenger, and A. F. Koenderink, ACS Nano **7**(10), 8840–8848 (2013), PMID: 24020654.
[25] P. Nordlander, , C. Oubre, E. Prodan, K. Li, , and M. I. Stockman, Nano Letters **4**(5), 899–903 (2004).
[26] E. Prodan and P. Nordlander, The Journal of Chemical Physics **120**(11), 5444–5454 (2004).
[27] I. Sersic, C. Tuambilangana, and A. F. Koenderink, New Journal of Physics **13**(8), 083019 (2011).
[28] W. Lukosz and R. E. Kunz, J. Opt. Soc. Am. **67**(12), 1615–1619 (1977).
[29] L. Novotny and B. Hecht, Principles of nano-optics (Cambridge university press, 2012).
[30] H. P. Urbach and G. L. J. A. Rikken, Phys. Rev. A **57**(May), 3913–3930 (1998).
[31] Supplementary information.
[32] M. Cotrufo, C. I. Osorio, and A. F. Koenderink, ACS Nano **10**(3), 3389–3397 (2016), PMID: 26854880.
[33] A. H. Schokker and A. F. Koenderink, Phys. Rev. B **90**(Oct), 155452 (2014).
[34] Q. Sun, Y. A. Wang, L. S. Li, D. Wang, T. Zhu, J. Xu, C. Yang, and Y. Li, Nat Photon **1**(12), 717–722 (2007).
[35] P. O. Anikeeva, J. E. Halpert, M. G. Bawendi, and V. Bulovi, Nano Lett. **9**(7), 2532–2536 (2009), PMID: 19514711.
[36] J. M. Caruge, J. E. Halpert, V. Wood, V. Bulovic, and M. G. Bawendi, Nat Photon **2**(4), 247–250 (2008).
[37] S. Coe, W. K. Woo, M. Bawendi, and V. Bulovic, Nature **420**(6917), 800–803 (2002).
[38] M. Florescu, P. J. Steinhardt, and S. Torquato, Phys. Rev. B **87**(Apr), 165116 (2013).
[39] A. Utgenannt, R. Maspero, A. Fortini, R. Turner, M. Florescu, C. Jeynes, A. G. Kanaras, O. L. Muskens, R. P. Sear, and J. L. Keddie, ACS Nano **10**(2), 2232–2242 (2016), PMID: 26767891.